

# Entropy Generation and Thermal Analysis of Nanofluid Flow Inside the Evacuated Tube Solar Collector

S. Mojtaba Tabarhoseini

Babol Noshirvani University of Technology

M. Sheikholeslami (✉ [mohsen.sheikholeslami@nit.ac.ir](mailto:mohsen.sheikholeslami@nit.ac.ir))

Babol Noshirvani University of Technology

---

## Research Article

**Keywords:** Evacuated tube solar collector, Thermal performance, Entropy generation, Nanofluid.

**Posted Date:** October 22nd, 2021

**DOI:** <https://doi.org/10.21203/rs.3.rs-967559/v1>

**License:** © ⓘ This work is licensed under a Creative Commons Attribution 4.0 International License. [Read Full License](#)

---

**Version of Record:** A version of this preprint was published at Scientific Reports on January 26th, 2022. See the published version at <https://doi.org/10.1038/s41598-022-05263-2>.

## Abstract

In the current investigation, the thermal and thermodynamic behavior of a buoyancy-driven evacuated tube solar collector has undergone precise evaluation, and the efficacy of nanoparticle dispersion in the base fluid has been scrutinized using computational fluid dynamics based on the finite volume method. The natural convection process was analyzed in different vertical sections of the absorber tube. The temperature and velocity distributions of water as the conventional working fluid and the nanofluid were compared at various cutting planes along the tube during the simulation time. In this problem, CuO nanoparticles with optimum thermal properties were suspended in the base fluid. According to the surveyed results, the temperature distribution analysis illustrates that the mean temperature of the tank experiences more enhancement when the nanofluid is used. The comparison of the heat transfer coefficient between two simulated cases shows the competency of utilizing CuO/water nanofluid in the thermal performance improvement of the collector. The results related to entropy generation assessment show that the irreversibility owing to fluid friction rises when the nanofluid is applied during the flow time. In contrast, the entropy generation of pure water owing to heat transfer surpasses the case with nanofluid.

## Introduction

Last decades have witnessed a burgeoning demand for energy consumption produced by fossil fuels, which in turn has led to growing concerns about environmental issues such as air pollution and other serious problems. Taking the limited resources of fossil fuels and their high cost as an example. Based on this fact, to alleviate deleterious efficacies in connection with it, researchers have focused their attention and dedicated their study to renewable energy resources. More specifically, solar energy, as one of the most promising types of clean energy, is utilized in a broad range of applications owing to its accessibility and innocuous usage [1, 2]. Solar water and air heaters, air conditioning systems, solar dryers, desalination systems, etc. are the most common exemplar of solar energy applications in industrial and residential sectors [3]. Solar water heating systems are sweepingly utilized as one of the most prevalent solar energy technologies, which can supply approximately 70% of residential or commercial water heating demand [4]. Evacuated tube and flat plate collectors are two types of stationary solar collectors by which solar energy can be captured to produce hot water. From a comparative point of view, evacuated tube collectors play a more significant role than flat plate collectors because they provide higher thermal efficiency at operating temperatures below 100°C [5]. ETSCs are composed of an absorber tube surrounded by two concentric glass tubes that are directly exposed to solar radiation. There is a vacuum envelope between the glass tube and absorber, leading to minimization of the heat loss originating from radiation and convection heat transfer [6]. Moreover, the absorbed heat is transferred to the working fluid inside the absorber tube by use of various heat extraction methods [7]. ETSCs are assorted into three types in terms of heat extraction techniques: heat-pipe ETSC, U-pipe ETSC, and water-in-glass ETSC [8]. Water-in-glass or thermosyphon models have been the center of attention of researchers by virtue of low maintenance cost, simplicity, and appropriate thermal performance [9]. Copious numerical and empirical investigations have been carried out studying the thermal functionality of ETSCs. The collector slope, mass flow rate, type of working fluids, inlet fluid temperature, and geometrical parameters are the most efficacious factors affecting the collector efficiency [10–12]. Alfaro-Ayala et al. [13] carried out an optimization for WIGETCs with steady-state and laminar regime using the CFD model and the simulated annealing method. With regard to the optimization analysis, the absorber area of the collector's commercial geometry has been 19.4% lower than that of the optimal geometry with a minimum absorber area of approximately 2.5 m<sup>2</sup>. Other optimum values, such as the number and length of vacuum tubes, were reduced by 40%, while the energy efficiency of the whole collector increased up to 26.3%. To increase the performance of the AGETC, Yao et al. [14] employed twisted tape inside a single-ended evacuated tube for various initial temperatures. The obtained results illustrated that using twist tape is effective in heat transfer augmentation at high initial temperatures. The intensification of solar radiation and its angle on the collector performance has been analyzed by Essa and Mostafa [15] in a numerical transient simulation considering a single-ended tube with a storage manifold. Based on the simulation results, variation of solar radiation intensity leads the flow structure to change from the linear profile to the helical form along the tube, which originates from movement of the sun rays. Alfaro-Ayala et al. [16] applied the Boussinesq approximation (BA) and the variation of the properties (VPT) approaches to evaluate the outlet temperature of fluid inside the storage tank of a WIGETC using CFD simulation. It has been reported that the collector efficiency and outlet fluid temperature were in closer concordance to the experimental data by utilization of the BA method compared to the VPT model. Mazarron et al. [17] evaluated the fluid flow, design and installation of a SWH system with an evacuated tube collector at various operational temperatures. It has been concluded that the highest efficiency of the proposed system obtained at 50°C water temperature, and the lowest thermal efficiency was for the case with 80°C inlet fluid temperature. Moreover, the profitability of the system decreases, while the operational temperature rises. Apart from all the contributing factors which can significantly improve the thermal performance of the system, using nanofluids is an efficacious technique, leading the solar collectors to have better thermal efficiency compared to conventional working fluids. Owing to the higher capability of nanofluids for carrying heat up in comparison with other typical fluids, the use of nanofluids has been prevalent in a broad range of applications, particularly in ETSCs. Nanofluids are prepared by dispersing nano-sized particles into the base fluids. Sharafeldin and Grof [18] used CeO<sub>2</sub>/water nanofluid with 3 volume concentration of 0.015%, 0.025% and 0.035% to examine the thermal functionality of the ETSC at various mass flux rates. Regarding the obtained results, using CeO<sub>2</sub>/water nanofluid with 0.035% volume fraction has shown the greatest influence on enhancing the thermal efficiency of the collector up to 34%. Ozsoy and Corumlu [19] analyzed the performance of a HPETC using silver-water nanofluid. They reported that the thermal efficiency of the proposed system raised in the range of 20%-40%, while using nanofluid in place of pure water. Gan et al. [20] found that employing TiO<sub>2</sub>-water nanofluid under optimum circumstances can lead the thermal efficiency of the ETSC to augment around 16.5% in comparison to the case with pure water. Dehaj and Mohiabadi [21] conducted an experimental study to evaluate the efficiency of HPETC by using MgO nanofluid at different volume fractions. They found that MgO/water nanofluid has a major impact on raising the thermal performance of the collector, while using instead of water. Moreover, increasing the concentration of the nanofluid can improve the collector's functionality. According to the observations of Yan et al. [22] in their empirical experiment, SiO<sub>2</sub>/water nanofluid at 5% mass fraction has shown its merits in improving the collector performance compared to plain water. Sharafeldin and Grof [23] demonstrated the significance and the efficacy of Cu/water nanofluid in ETSC, where different volume flow rates of the fluid and volume concentration of the nanoparticles were examined. The results have divulged that a 50% increment took place in the outlet temperature of the collector at volume concentration of 0.03% and volume flow rate of 0.8 L/min.

With regard to the second law of thermodynamics, the thermal efficiency of a system will experience a reduction over time, owing to the fact that heat energy conversion process is irreversible. The assessment of entropy generation in engineering applications was proposed by Bejan [24] as an efficacious way to justify the performance improvement in thermal systems, where there are limitations for energy analysis [25]. Employing nanofluids leads the entropy generation of the system to reduce [26]. There are few literatures in the field of ETSCs, which put their main focus on entropy generation and irreversibility. Based on the study carried out by Leong et al. [27], a comparison in terms of entropy generation has been drawn between  $\text{TiO}_2$  and  $\text{Al}_2\text{O}_3$  nanofluid inside a circular tube. Their observation has shown that the total entropy generation was higher for  $\text{Al}_2\text{O}_3$  nanofluid than that of  $\text{TiO}_2$  nanofluid. Ramirez-Minguela et al. [28] appraised the rate of entropy generation for FPC and ETSC using CFD simulation. The obtained results revealed that ETSC has higher thermal entropy generation than FPC by virtue of more heat transmission, which takes place in vacuum tube collector. In contrast, FPC has shown higher entropy generation due to the fluid friction.

According to the lack of researches focusing on the entropy generation assessment in solar collectors, particularly ETSCs, this study aims to analyze the entropy generation inside a single-ended ETSC with a comparative evaluation between two cases with using pure water and nanofluid as the heat transfer fluids over 1 hour of simulation time.  $\text{CuO}/\text{water}$  nanofluid has been selected with optimum properties as the heat transfer fluid. Entropy generation derived from fluid friction and heat transfer is examined and compared for both simulated cases. Moreover, for thermal evaluation of the proposed system, temperature and velocity distributions and contours inside the three cutting sections of the collector tube were analyzed for water and nanofluid, by which the merits of using the  $\text{CuO}$  nanofluid has been demonstrated.

## Physical Model And Formulation

The simulation process of the current study has been modelled for a close-ended thermosyphon ETSC along with the manifold investigating its thermal behavior and entropy generation. Fig. 1 provides an overview of the geometry of the simulated model. As shown in the figure, the absorber tube has been divided into three vertical sections aim to analyze the fluid flow array along the tube, from the entrance to the close-end. The absorber tube has been considered with the slope of  $45^\circ$  through the z direction. The dimensions of the proposed system are provided in Table 1. The fluid flow simulation process was carried out using ANSYS FLUENT software by utilization of the FVM method. The SIMPLE algorithm was used for the coupling of velocity and pressure in the governing equations. The momentum and energy equations were discretized by the second-order upwind method. What's more, the Boussinesq approximation method is used for density difference consideration as a result of the slope of the absorber tube. The main assumptions for the fluid flow structure are incompressible, laminar, and continuous. To reduce the computational time and regarding the solution process, which is time dependent (transient), the simulation flow time has been considered for 1 hour.

### 2.1. Mesh structure, initial, and boundary conditions

Mesh structure is one of the effective elements in CFD simulations, on which the accuracy of the results is based. In the current study, the average tank temperature in different cases with various numbers of nodes varying from 258743 to approximately 500000 was compared to reach the optimum number of nodes to reduce computational cost and time. It has been concluded that when the number of nodes surpasses 380000, the changes in the results are trivial and negligible. Hence, 380675 nodes were specified as the extra fine mesh for the simulation process. In addition, the value of skewness was 0.17, which shows the high quality of the mesh structure. The shape of the grid used in this study is shown in Fig. 2.

The entire system is composed of two main components: the storage tank, which has heat exchange with the environment with the heat transfer coefficient of  $8 \text{ W/m}^2 \cdot \text{K}$ , and the absorber tube, which is at the direct exposure of solar radiation. In order to simulate solar radiation at the simulation time, a constant heat flux of  $900 \text{ W/m}^2$  has been considered. As shown in Fig. 1, a quarter of the top surface of the absorber is determined as the surface on which the solar flux is defined, while other surfaces of the absorber are considered as adiabatic walls. For the initial conditions, the initial velocity, and the initial temperature of the fluid were assumed to be zero and  $25^\circ\text{C}$ , respectively. Last but not least, to decrease the computational cost and complexity of the solution, the outer glass tube along with the vacuum envelope between the glass cover and the absorber tube has been neglected. In order to take the results closer to the real case, the effects of eliminated parts have been taken into consideration in boundary conditions [29, 30].

### 2.2. Validation and time step independence

Proving the accuracy of the results is an important part of a numerical simulation. Because of this, the experimental and the numerical study conducted by Jowzi et al. [31] has been selected to verify the simulation in the present model. As it is depicted in Table 2, the obtained values for the tank's mean temperature over 1 hour of simulation are in good concordance with the numerical and empirical results, with an error of less than 3% in both studies, which shows the authenticity of the current results.

Choosing an appropriate size for the time step in the simulation process can be helpful to reduce the computational time and simultaneously give accurate results. Fig. 3 illustrates the time step analysis considering the mean temperature of the absorber and tank during 1 hour of the simulation process. As is obvious, at a 5 second time step size, the mean temperature of the tube and tank witnesses a significant difference from the results obtained at two other time steps after 25 and 15 minutes of flow time, respectively. Thus, a time step size of 2 seconds is acceptable for use in the numerical simulation process.

### 2.3. Mathematical modelling

In order to consider lifting efficacy in the simulation process, Boussinesq approximation model has been taken into account. In this approach, density is considered as the variable parameter, while all other thermophysical and transport characteristics are assumed constant. It is stated in terms of thermal expansion coefficient ( $\beta$ ) and temperature (T), which is expressed as follows:

$$\rho_{\infty} - \rho = \rho\beta(T - T_{\infty}) \quad (1)$$

where  $\beta$  is the denotation of the volume expansion coefficient with a constant value of  $0.000344\text{K}^{-1}$ , as shown in Table 3. Considering the buoyancy effect in the conservation equations leads to the equations given below. The continuity equation for the laminar flow regime is defined as follows:

$$\rho \left( \frac{\partial u_x}{\partial x} + \frac{\partial u_y}{\partial y} + \frac{\partial u_z}{\partial z} \right) = 0 \quad (2)$$

The momentum equations are categorized into x, y, and z components:

x-component:

$$u_x \frac{\partial u_x}{\partial x} + u_y \frac{\partial u_x}{\partial y} + u_z \frac{\partial u_x}{\partial z} = -\frac{1}{\rho} \frac{\partial p}{\partial x} + \frac{\mu}{\rho} \left( \frac{\partial^2 u_x}{\partial x^2} + \frac{\partial^2 u_x}{\partial y^2} + \frac{\partial^2 u_x}{\partial z^2} \right) \quad (3)$$

y-component:

$$u_x \frac{\partial u_y}{\partial x} + u_y \frac{\partial u_y}{\partial y} + u_z \frac{\partial u_y}{\partial z} = g_y \beta (T - T_{\infty}) + \frac{\mu}{\rho} \left( \frac{\partial^2 u_y}{\partial x^2} + \frac{\partial^2 u_y}{\partial y^2} + \frac{\partial^2 u_y}{\partial z^2} \right) \quad (4)$$

z-component:

$$u_x \frac{\partial u_z}{\partial x} + u_y \frac{\partial u_z}{\partial y} + u_z \frac{\partial u_z}{\partial z} = -\frac{1}{\rho} \frac{\partial p}{\partial z} + \frac{\mu}{\rho} \left( \frac{\partial^2 u_z}{\partial x^2} + \frac{\partial^2 u_z}{\partial y^2} + \frac{\partial^2 u_z}{\partial z^2} \right) \quad (5)$$

Energy equation:

$$\rho c \left( u_x \frac{\partial T}{\partial x} + u_y \frac{\partial T}{\partial y} + u_z \frac{\partial T}{\partial z} \right) = k \left( \frac{\partial^2 T}{\partial x^2} + \frac{\partial^2 T}{\partial y^2} + \frac{\partial^2 T}{\partial z^2} \right) \quad (6)$$

In our study, the suspension of nanoparticles inside pure water was assumed to be the single-phase approach. In detail, nanoparticles are homogenously dispersed into the base fluid. The formulations related to the nanofluid modeling that are applied in this problem are described by the following equations [32]:

Density:

$$\rho_{nf} = (1 - \varphi)\rho_f + \varphi\rho_s \quad (7)$$

Heat capacity:

$$(\rho c_p)_{nf} = (1 - \varphi)(\rho c_p)_f + \varphi(\rho c_p)_s \quad (8)$$

Viscosity:

$$\mu_{nf} = \frac{\mu_f}{(1 - \varphi)^{2.5}} \quad (9)$$

Thermal conductivity:

$$\frac{k_{nf}}{k_f} = \frac{k_s + 2k_f - 2\varphi(k_f - k_s)}{k_s + 2k_f - \varphi(k_f - k_s)} \quad (10)$$

Thermal expansion coefficient:

$$\beta_{nf} = \left[ \frac{1}{1 + \frac{\varphi \rho_s}{(1 - \varphi)\rho_f}} \frac{\beta_s}{\beta_f} + \frac{1}{1 + \frac{\varphi \rho_s}{1 - \varphi \rho_f}} \right] \beta_f \quad (11)$$

The thermophysical characteristics of CuO nanoparticles were calculated using the above equations, as shown in Table 3. The heat transfer coefficient is obtained to estimate the thermal performance of the system, which is defined as:

$$h = \frac{q''}{(T_w - T_b)} \quad (12)$$

Turning to the focus of this study, entropy generation analysis has been carried out in order to assess the functionality of the proposed system. The rate of local entropy generation can be calculated from the velocity and temperature fields gained from the CFD analysis by utilization of the thermodynamics second law. The total rate of entropy generation is defined with the summation of fluid friction and heat transfer irreversibility [33]:

$$S_{gen,l} = S_{gen,lth} + S_{gen,lf} = \frac{k_{nf}}{T^2} \left[ \left( \frac{\partial T}{\partial x} \right)^2 + \left( \frac{\partial T}{\partial y} \right)^2 + \left( \frac{\partial T}{\partial z} \right)^2 \right] + \frac{\mu_{nf}}{T} \left[ 2 \left[ \left( \frac{\partial u_x}{\partial x} \right)^2 + \left( \frac{\partial u_y}{\partial y} \right)^2 + \left( \frac{\partial u_z}{\partial z} \right)^2 \right] + \left[ \left( \frac{\partial u_x}{\partial y} + \frac{\partial u_y}{\partial x} \right)^2 + \left( \frac{\partial u_x}{\partial z} + \frac{\partial u_z}{\partial x} \right)^2 + \left( \frac{\partial u_y}{\partial z} + \frac{\partial u_z}{\partial y} \right)^2 \right] \right] \quad (13)$$

where *lf* and *lth* denote local entropy generation due to the friction of fluid and heat transfer, respectively. With regard to the nanofluid flow equations, the correlations related to entropy generation can be defined as:

$$S_{gen,lf} = \int \{S_{gen,lf}\} dV, S_{gen,lth} = \int \{S_{gen,lth}\} dV \quad (14)$$

**Table 1.** Geometrical parameters

Parameter	Value
Absorber Length (a,b)	a = 250 cm b = 500 mm
Absorber diameter (d)	4.5 cm
Manifold length	10 cm
Manifold diameter	20 cm
Collector slope	45°
Heat flux (q)	900 W/m <sup>2</sup>

**Table 2.**

Comparison of the tank temperature of the present model with numerical and experimental data [31]

Time (min)	T <sub>a</sub> (k) experimental by Jowzi et al. [31] (°C)	T <sub>a</sub> (k) numerical by Jowzi et al. [31] (°C)	T <sub>a</sub> (k) present study (°C)	Error (%) with numerical data	Error with experimental data
15	33.43	32.90	32.46	1.34	2.9
30	34.71	34.78	34.71	0.21	0.0
45	36.37	36.370	36.92	0.6	1.5
60	37.96	38.58	39.20	1.62	3.2

**Table 3.** Thermophysical properties of water and CuO nanoparticles used in this study

	ρ (kg/m <sup>3</sup> )	Cp (J/kg k)	K (W/m k)	μ (kg/ms)	β (1/K)
Water (30°C)	997.1	4179	0.613	0.001	0.000344
CuO	6500	540	18	—	0.00029

## Results And Discussion

### 3.1. Thermal analysis

This section delineates the impacts of nanofluid convective flow and entropy generation inside a single-ended evacuated tube solar collector. The collector tube has been divided into three sections by vertical lines (lines 1, 2, and 3), each of which was surrounded by cutting planes. In order to reduce computational cost, the numerical simulation results have been considered for 1 hour of flow time, which can be extended to a one-day duration. In the first step, the velocity distributions of fluid flow with plain water and nanofluid are compared in the entire tube and each cutting section after 30 and 60 minutes, respectively. In the second step, the same comparative analysis has been conducted for the temperature range inside the tube and storage tank for both fluid flows. Finally, entropy generation assessment is carried out for both cases during the simulation time along the tube.

To elaborate on the entire natural circulation procedure taking place inside the tube, at the beginning of the process, cold fluid flows from the storage tank toward the close-ended side of the tube. Meanwhile, the top surface of the tube, which is at the direct exposure of solar radiation, is involved in absorbing and transferring the absorbed heat to the working fluid flowing through the tube. While the absorbed heat is transmitted to the working fluid, the change in density engenders the buoyancy effect, which eventually leads the fluid to experience a natural circulation process and moves from the tube toward the reservoir, and vice versa, as shown in Fig. 4(a) and (b). As it is obvious in Fig. 4, the fluid flow inside the tube is divided into layers of cold and warm water at the bottom and top halves of the tube, which are clearly separated. Fig. 5(a) and (b) demonstrate the velocity magnitudes inside the tube and tank for the nanofluid at 0.5 and 1 hour of simulation. From a comparative viewpoint, the velocity range for water as the base fluid is marginally lower than that of the case with nanofluid.

Fig. 6(a) and (b) comparatively analyze the velocity magnitudes of different vertical planes of lines 1, 2 and 3 during the passage of flow time. At  $t=0.5$  hours of flow time, it is observable that a slight discrepancy in velocity values occurs between the two simulated cases in the regions of  $(-0.02\text{ m}, -0.015\text{ m})$  and  $(0.015\text{ m}, 0.02\text{ m})$  along the vertical sections for all three lines. The negative velocity values denote the fluid flow in the direction toward the tube's close end, while the positive values refer to the outflow which is moving toward the manifold in the form of natural convection. Among all the cutting sections, the least difference in velocity magnitudes for both cases are existed in line 3, which is near the stagnant region at the end of the tube, leading the fluid flow to have the lowest rate of velocity compared with the line near the entry region. On the contrary, the utmost velocity difference of water and nanofluid appertain to line 1, where the fluid flows with the maximum velocity. The last point which can be deduced from Fig. 6(a) is that line 1 reached the highest peak point of velocity, and as the vertical planes approach the tube's end, the peak point starts to decrease. This is due to the fact that when water enters the tube sliding layer, which has the lowest speed starts to form near the bottom and top surfaces of the tube wall owing to the opposite direction of fluid flow in these regions, which leads to a reduction in the peak velocity. Fig. 6(b) compares the velocity distribution for the pure water and nanofluid cases at  $t=1$  hour. Despite the marginal velocity differences of nanofluid and water in different sections at  $t=0.5$  hours, more differences were observed in the vertical planes of line 1 and line 2, although they remained roughly unchanged in line 3 as the flow time increased up to 1 hour. Moreover, the velocity values of water and nanofluid observed to have more differences between the highest and lowest peak points of velocity compared to other regions in all the sections. What stands out, the outflow velocity of the nanofluid in line 1 (starting at  $Y=-0.019$ ) was found to have higher quantities in comparison to the case with plain water. All things considered, the velocity values for the nanofluid stood at approximately  $40\text{ mm/s}$  in line 1 at the peak point ( $Y=0.018$ ) for  $t=1$  hour, which was the highest magnitude among all other sections. The procedure of fluid circulation is obviously illustrated in temperature distributions for water and nanofluid over the simulation time in Figs. 7 and 8. To be more precise, the bottom region of the tank, which encompasses fluid with lower temperature, flows down to the tube, and the fluid turning back to the manifold flows faster due to the viscosity decrement as a result of temperature enhancement. Furthermore, the natural circulation rate faces a reduction near the close end of the tube. Fig. 9 depicts the temperature profile inside the specified sections of the tube for water and nanofluid after 0.5 and 1 hour. It is deduced that the inflow which is flowing from the manifold toward the tube has a considerably lower temperature than the outflow that returns toward the reservoir. After a 30-minute simulation period, the temperature difference between the water and nanofluid remained marginal in all the regions of the cutting planes, while this difference was augmented over the flow time passage. Hence, it can be concluded that using a nanofluid has a considerable effect on the thermal performance of the collector specifically when the simulation time is extended to 1 day. Among all three sections for the simulated cases, the utmost temperature magnitudes have been obtained for the nanofluid in the first plane at  $t=60$  minutes. It is noteworthy to mention that the temperature increment by utilizing nanofluid is observable in the regions from  $Y=-0.013$  to  $0.013$  at 1 hour after simulation time. The last outstanding feature of this process, which can be seen in the figure, is the intensification of temperature augmentation starting from  $Y=0.013$  to the top surface of the absorber tube compared to other regions. This fact can be justifiable when the secondary flow, which originates from the inflow, joins the outflow and its temperature undergoes enhancement. As can be seen in Fig. 10, the heat transfer coefficient has been calculated in order to make a comparison between the two simulated cases and show the merit of using nanofluid on the thermal performance of the collector. It is clear that the heat transfer coefficient for the case with nanofluid is higher than that of conventional fluid over the simulation time.

### 3.2. Entropy generation analysis

Besides the thermal assessment aimed at exploring the impact of nanofluid as the working fluid in the collector, an entropy generation analysis is provided for both cases over the simulated flow time in order to compare the behavior of the irreversibility in the system under the simulated cases. Fluid friction ( $\dot{S}_{gen,f}$ ) and heat transfer ( $\dot{S}_{gen,th}$ ) were two factors of entropy generation, which has been considered in this study using the formulation of Eq. 14. Fig. 11(a) and (c) illustrate the distribution of entropy generation for pure water due to fluid viscosity, and Fig. 11(b) and (d) illustrate the distribution of entropy generation for pure water due to heat transfer throughout the collector tube and manifold at  $t=0.5$  hours and  $t=1$  hour of flow time. It can also be inferred that the upper surface of the tube, which is exposed to constant heat flux, experiences the utmost heat transfer entropy generation owing to the maximum temperature gradient between the working fluid and the walls of these surfaces. Additionally, the maximum fluid friction entropy generation is observable near the top surface of the tube wall and a part of the manifold, where the outflow possesses the maximum velocity magnitude. Fig. 12(a) and (c) depict the distribution of fluid friction entropy generation for the nanofluid over the flow time inside the tube. It can be seen that the motion of inflow and outflow near the bottom and top surfaces of the tube, which originate from natural convection, have a homogenous distribution. Fig. 12(b) and (c) show the distribution of thermal entropy generation for the nanofluid over the flow time. It is worth pointing out that the high values of entropy generation near the top wall illustrate the maximum value of the temperature gradient between the fluid and the tube's surface. Fig. 13(a) and (b) illustrate the comparison of the fluid friction entropy generation and the thermal irreversibility for the conventional fluid and the nanofluid during the simulation time. It is observable that the use of nanofluid leads the fluid friction irreversibility to enhance, whereas heat transfer entropy generation reduces by using nanofluid as the heat transfer fluid. Heat transfer irreversibility reduction by utilization of the nanofluid belies in the fact that the finite temperature difference is lower, while the heat transfer of the system faces an improvement with the aid of nanofluid. Turning to the other side, pressure drop increases when the nanofluid is used in the system, which in turn leads to fluid friction augmentation. Notably, the heat transfer entropy generation is considerably higher than that of fluid friction entropy generation when the fluid possesses low velocity.

### Conclusion

The lack of meticulous studies fixated on the thermodynamic scrutinization of evacuated tube collectors by the presence of nanofluids as an effective heat transfer fluid in the thermal performance improvement of the system was the main reason this study was carried out. Moreover, the proposed system has undergone thermal evaluation to analyze the fluid structure inside the system and the desirability of the nanofluid flow to enhance the performance of the collector. To verify the results of the present model, experimental and numerical studies were chosen to certify the authenticity of this research and its results. The dispersion of CuO nanomaterials at a 5% volume fraction in plain water was selected in this study according to its merit and had the utmost impact on the collector's thermal performance improvement compared to all other types of nanoparticles, which led to several changes in the performance of the system. First, the suspension of nanoparticles in the testing fluid caused the fluid temperature to increase. More importantly, as the simulation time increases from 0 to

60 minutes, the temperature difference between the case with nanofluid and the case with pure water starts to increase. Second, the heat transfer coefficient comparison, which has been drawn between the two simulated cases, denotes the thermal superiority of nanofluid flow in the system. Ultimately, the entropy generation examination as the main objective of this study has shown that adding CuO nanoparticles is a contributing factor, affecting the heat transfer irreversibility to endure a reduction compared to the one with conventional fluid. It is noteworthy to mention that fluid friction entropy generation was found to have minuscule values in both cases, showing the irrelevancy of the fluid flow viscous stresses. Overall, a higher total entropy generation rate was obtained for the typical type of collector with pure water.

## Abbreviations

AGETC		$S_{gen,th}$	Entropy generation due to heat transfer (W/K)
BA	Boussinesq approximation	$T$	Temperature (K)
CFD	Computational fluid dynamics	$T_b$	Bulk temperature (K)
ETSC	Evacuated tube solar collector	$T_w$	Wall temperature (K)
FPC	Flat plate collector	$T_{ave}$	The average temperature (K)
SWH	Solar water heating	$t$	Time (sec)
VPT	Variable properties temperature		
WIGETC	Water-in-glass evacuated tube collector		
		<i>Greek</i>	
		$\beta$	thermal expansion coefficient (1/K)
		$\theta$	tilt angle of the tube
		$\mu$	dynamic viscosity (Pa s)
		$\rho$	density (kg/m <sup>3</sup> )
		$\rho_0$	density of fluid at initial temperature (kg/m <sup>3</sup> )
		$\varphi$	volume fraction
		<i>Subscripts</i>	
		$f$	fluid
		$l$	Local
		$nf$	nanofluid
		$s$	nanoparticle
<i>Symbols</i>			
$b$	tank length (mm)		
$c_p$	specific heat capacity (J/kg K)		
$D$	tank diameter (mm)		
$d$	Absorber diameter (mm)		
$g$	gravitational acceleration (m/s <sup>2</sup> )		
$k$	thermal conductivity (W/m K)		
$q$	Constant heat flux (W/m <sup>2</sup> )		
$S_{gen}$	Total entropy generation (W/K)		
$S_{gen,f}$	Entropy generation due to fluid friction (W/K)		

## References

- [1] Martinopoulos G, Tsilingiridis G, Kyriakis N. Identification of the environmental impact from the use of different materials in domestic solar hot water systems. *Appl Energy* 2013;102:545–55. <https://doi.org/10.1016/J.APENERGY.2012.08.035>.
- [2] Comodi G, Bevilacqua M, Caresana F, Pelagalli L, Venella P, Paciarotti C. LCA Analysis of Renewable Domestic Hot Water Systems with Unglazed and Glazed Solar Thermal Panels. *Energy Procedia* 2014;61:234–7. <https://doi.org/10.1016/J.EGYPRO.2014.11.1096>.
- [3] Shah TR, Ali HM. Applications of hybrid nanofluids in solar energy, practical limitations and challenges: A critical review. *Sol Energy* 2019;183:173–203. <https://doi.org/10.1016/J.SOLENER.2019.03.012>.
- [4] Coimbra J, Almeida M. Challenges and benefits of building sustainable cooperative housing. *Build Environ* 2013;62:9–17. <https://doi.org/10.1016/J.BUILDENV.2013.01.003>.
- [5] Eidan AA, AlSahlani A, Ahmed AQ, Al-fahham M, Jalil JM. Improving the performance of heat pipe-evacuated tube solar collector experimentally by using Al2O3 and CuO/acetone nanofluids. *Sol Energy* 2018;173:780–8. <https://doi.org/10.1016/J.SOLENER.2018.08.013>.
- [6] Chopra K, Pathak AK, Tyagi V V, Pandey AK, Anand S, Sari A. Thermal performance of phase change material integrated heat pipe evacuated tube solar collector system: An experimental assessment. *Energy Convers Manag* 2020;203:112205. <https://doi.org/10.1016/J.ENCONMAN.2019.112205>.
- [7] Jowzi M, Veysi F, Sadeghi G. Experimental and numerical investigations on the thermal performance of a modified evacuated tube solar collector: Effect of the bypass tube. *Sol Energy* 2019;183:725–37. <https://doi.org/10.1016/J.SOLENER.2019.03.063>.
- [8] Yurddaş A. Optimization and thermal performance of evacuated tube solar collector with various nanofluids. *Int J Heat Mass Transf* 2020;152:119496. <https://doi.org/10.1016/J.IJHEATMASSTRANSFER.2020.119496>.
- [9] Zhang X, You S, Xu W, Wang M, He T, Zheng X. Experimental investigation of the higher coefficient of thermal performance for water-in-glass evacuated tube solar water heaters in China. *Energy Convers Manag* 2014;78:386–92. <https://doi.org/10.1016/J.ENCONMAN.2013.10.070>.
- [10] Naik BK, Bhowmik M, Muthukumar P. Experimental investigation and numerical modelling on the performance assessments of evacuated U – Tube solar collector systems. *Renew Energy* 2019;134:1344–61. <https://doi.org/10.1016/J.RENENE.2018.09.066>.
- [11] Mercan M, Yurddaş A. Numerical analysis of evacuated tube solar collectors using nanofluids. *Sol Energy* 2019;191:167–79. <https://doi.org/10.1016/J.SOLENER.2019.08.074>.
- [12] Li Q, Gao W, Lin W, Liu T, Zhang Y, Ding X, et al. Experiment and simulation study on convective heat transfer of all-glass evacuated tube solar collector. *Renew Energy* 2020;152:1129–39. <https://doi.org/10.1016/J.RENENE.2020.01.089>.
- [13] Alfaro-Ayala JA, López-Núñez OA, Gómez-Castro FI, Ramírez-Minguela JJ, Uribe-Ramírez AR, Belman-Flores JM, et al. Optimization of a solar collector with evacuated tubes using the simulated annealing and computational fluid dynamics. *Energy Convers Manag* 2018;166:343–55. <https://doi.org/10.1016/j.enconman.2018.04.039>.

- [14] Yao K, Li T, Tao H, Wei J, Feng K. Performance Evaluation of All-glass Evacuated Tube Solar Water Heater with Twist Tape Inserts Using CFD. *Energy Procedia* 2015;70:332–9. <https://doi.org/10.1016/j.egypro.2015.02.131>.
- [15] Essa MA, Mostafa NH. Theoretical and experimental study for temperature distribution and flow profile in all water evacuated tube solar collector considering solar radiation boundary condition. *Sol Energy* 2017;142:267–77. <https://doi.org/10.1016/j.solener.2016.12.035>.
- [16] Alfaro-ayala JA, Martínez-rodríguez G, Picón-núñez M, Uribe-ramírez AR, Gallegos-muñoz A. Numerical study of a low temperature water-in-glass evacuated tube solar collector. *Energy Convers Manag* 2015;94:472–81. <https://doi.org/10.1016/j.enconman.2015.01.091>.
- [17] Mazarrón FR, Porras-Prieto CJ, García JL, Benavente RM. Feasibility of active solar water heating systems with evacuated tube collector at different operational water temperatures. *Energy Convers Manag* 2016;113:16–26. <https://doi.org/10.1016/J.ENCONMAN.2016.01.046>.
- [18] Sharafeldin MA. Evacuated tube solar collector performance using CeO<sub>2</sub> / water nano fluid 2018;185:2–11. <https://doi.org/10.1016/j.jclepro.2018.03.054>.
- [19] Ozsoy A, Corumlu V. Thermal performance of a thermosyphon heat pipe evacuated tube solar collector using silver-water nanofluid for commercial applications. *Renew Energy* 2018;122:26–34. <https://doi.org/10.1016/J.RENENE.2018.01.031>.
- [20] Gan YY, Ong HC, Ling TC, Zulkifli NWM, Wang CT, Yang YC. Thermal conductivity optimization and entropy generation analysis of titanium dioxide nanofluid in evacuated tube solar collector. *Appl Therm Eng* 2018;145:155–64. <https://doi.org/10.1016/J.APPLTHERMALENG.2018.09.012>.
- [21] Dehaj MS, Mohiabadi MZ. Experimental investigation of heat pipe solar collector using MgO nanofluids. *Sol Energy Mater Sol Cells* 2019;191:91–9. <https://doi.org/10.1016/J.SOLMAT.2018.10.025>.
- [22] Yan S, Wang F, Shi ZG, Tian R. Heat transfer property of SiO<sub>2</sub>/water nanofluid flow inside solar collector vacuum tubes. *Appl Therm Eng* 2017;118:385–91. <https://doi.org/10.1016/J.APPLTHERMALENG.2017.02.108>.
- [23] Sharafeldin MA, Gróf G, Abu-Nada E, Mahian O. Evacuated tube solar collector performance using copper nanofluid: Energy and environmental analysis. *Appl Therm Eng* 2019;162:114205. <https://doi.org/10.1016/J.APPLTHERMALENG.2019.114205>.
- [24] Bejan A. A Study of Entropy Generation in Fundamental Convective Heat Transfer. *J Heat Transfer* 1979;101:718–25. <https://doi.org/10.1115/1.3451063>.
- [25] Kaushik SC, Reddy VS, Tyagi SK. Energy and exergy analyses of thermal power plants: A review. *Renew Sustain Energy Rev* 2011;15:1857–72. <https://doi.org/10.1016/J.RSER.2010.12.007>.
- [26] López A, Ibáñez G, Pantoja J, Moreira J, Lastres O. Entropy generation analysis of MHD nanofluid flow in a porous vertical microchannel with nonlinear thermal radiation, slip flow and convective-radiative boundary conditions. *Int J Heat Mass Transf* 2017;107:982–94. <https://doi.org/10.1016/J.IJHEATMASSTRANSFER.2016.10.126>.
- [27] Leong KY, Saidur R, Mahlia TMI, Yau YH. Entropy generation analysis of nanofluid flow in a circular tube subjected to constant wall temperature. *Int Commun Heat Mass Transf* 2012;39:1169–75. <https://doi.org/10.1016/J.ICHEATMASSTRANSFER.2012.06.009>.
- [28] Ramírez-Minguela JJ, Alfaro-Ayala JA, Rangel-Hernández VH, Uribe-Ramírez AR, Mendoza-Miranda JM, Pérez-García V, et al. Comparison of the thermo-hydraulic performance and the entropy generation rate for two types of low temperature solar collectors using CFD. *Sol Energy* 2018;166:123–37. <https://doi.org/10.1016/J.SOLENER.2018.03.050>.
- [29] Xu L, Wang Z, Yuan G, Li X, Ruan Y. A new dynamic test method for thermal performance of all-glass evacuated solar air collectors. *Sol Energy* 2012;86:1222–31. <https://doi.org/10.1016/J.SOLENER.2012.01.015>.
- [30] Sato AI, Scalón VL, Padilha A. Numerical analysis of a modified evacuated tubes solar collector. *Renew Energy Power Qual J* 2012;1:384–9. <https://doi.org/10.24084/repqj10.322>.
- [31] Jowzi M, Veysi F, Sadeghi G. Experimental and numerical investigations on the thermal performance of a modified evacuated tube solar collector: Effect of the bypass tube. *Sol Energy* 2019;183:725–37. <https://doi.org/10.1016/j.solener.2019.03.063>.
- [32] Bellos E, Tzivanidis C, Papadopoulos A. Enhancing the performance of a linear Fresnel reflector using nanofluids and internal finned absorber. *J Therm Anal Calorim* 2019;135:237–55. <https://doi.org/10.1007/s10973-018-6989-1>.
- [33] Bejan A, Kestin J. Entropy Generation Through Heat and Fluid Flow. *J Appl Mech* 1983;50:475–475. <https://doi.org/10.1115/1.3167072>.

## Figures

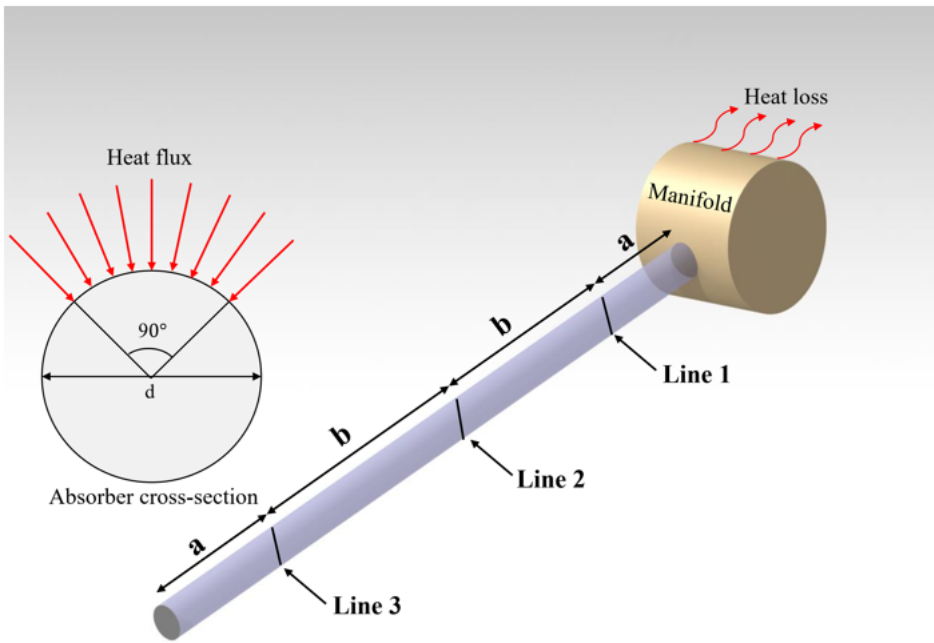


Figure 1

Geometry of the model

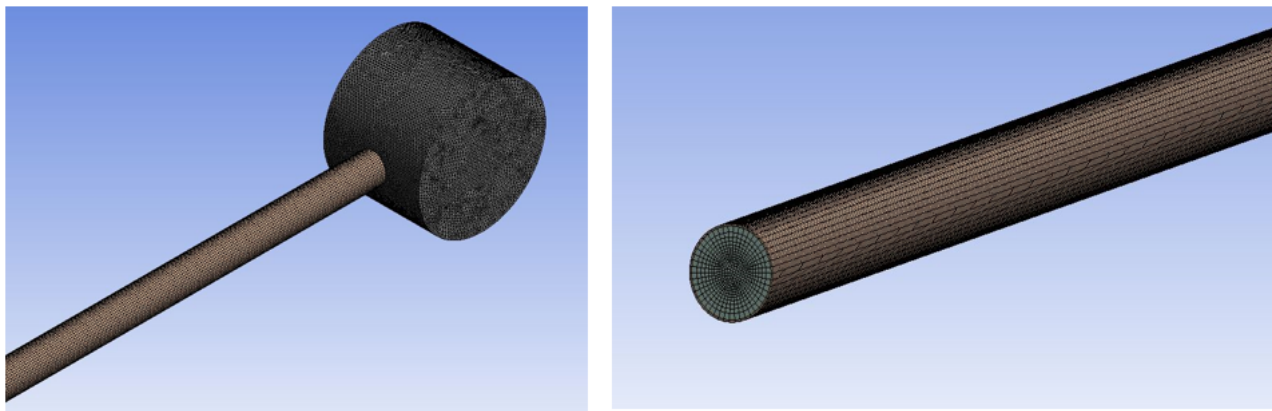


Figure 2

Mesh structure

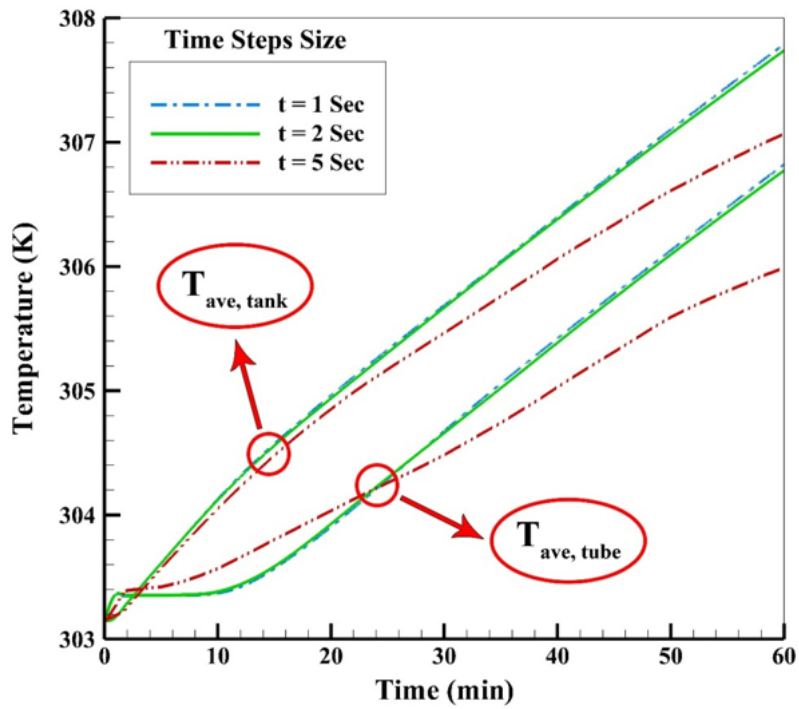


Figure 3

Time step independence for the mean temperature of the absorber and tank

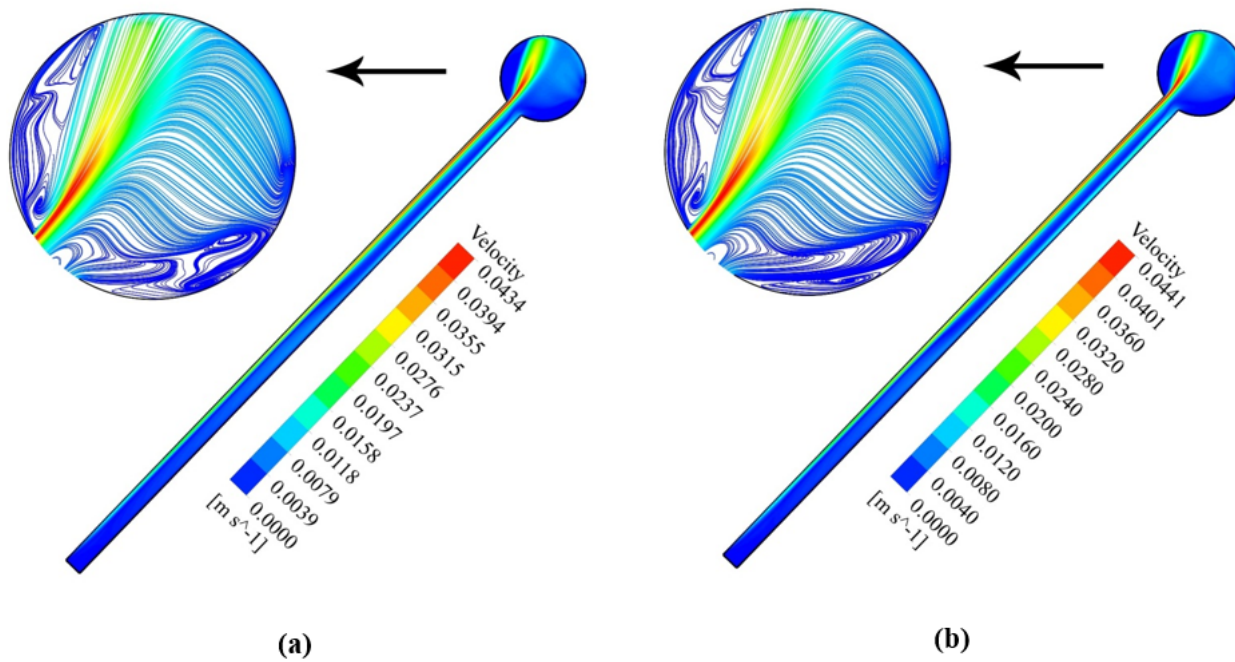


Figure 4

Distribution of velocity for water at (a)  $t=30$  and (b)  $t=60$  minutes

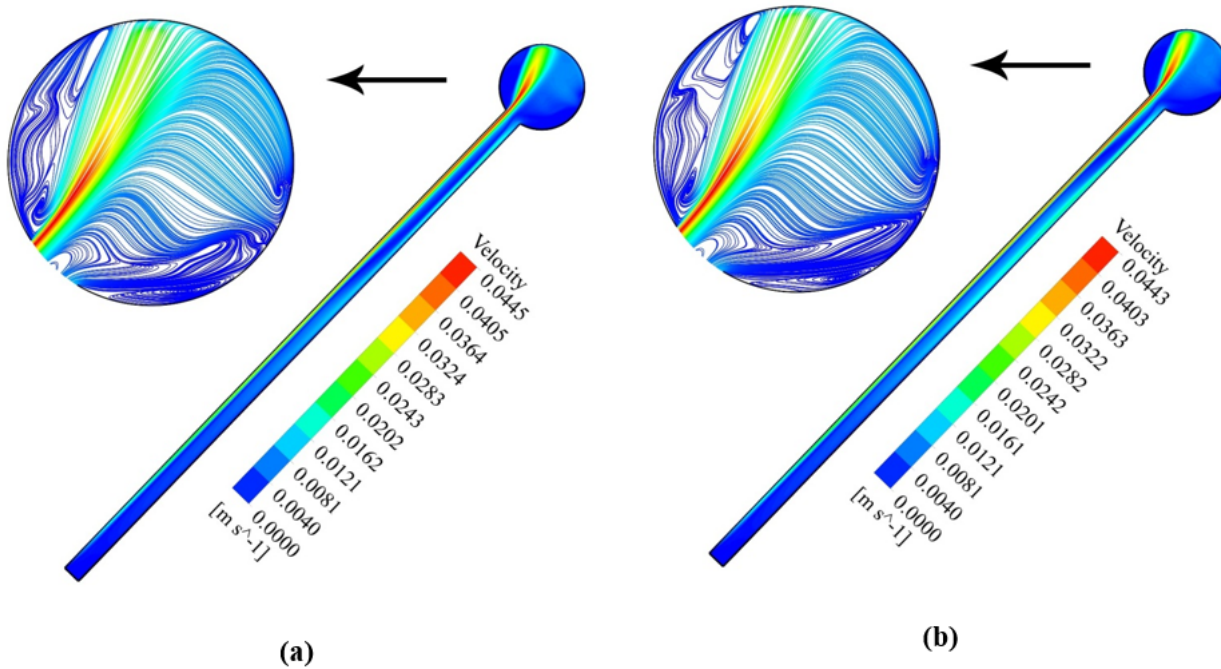


Figure 5

Distribution of velocity for nanofluid at (a) t=30 and (b) t=60 minutes

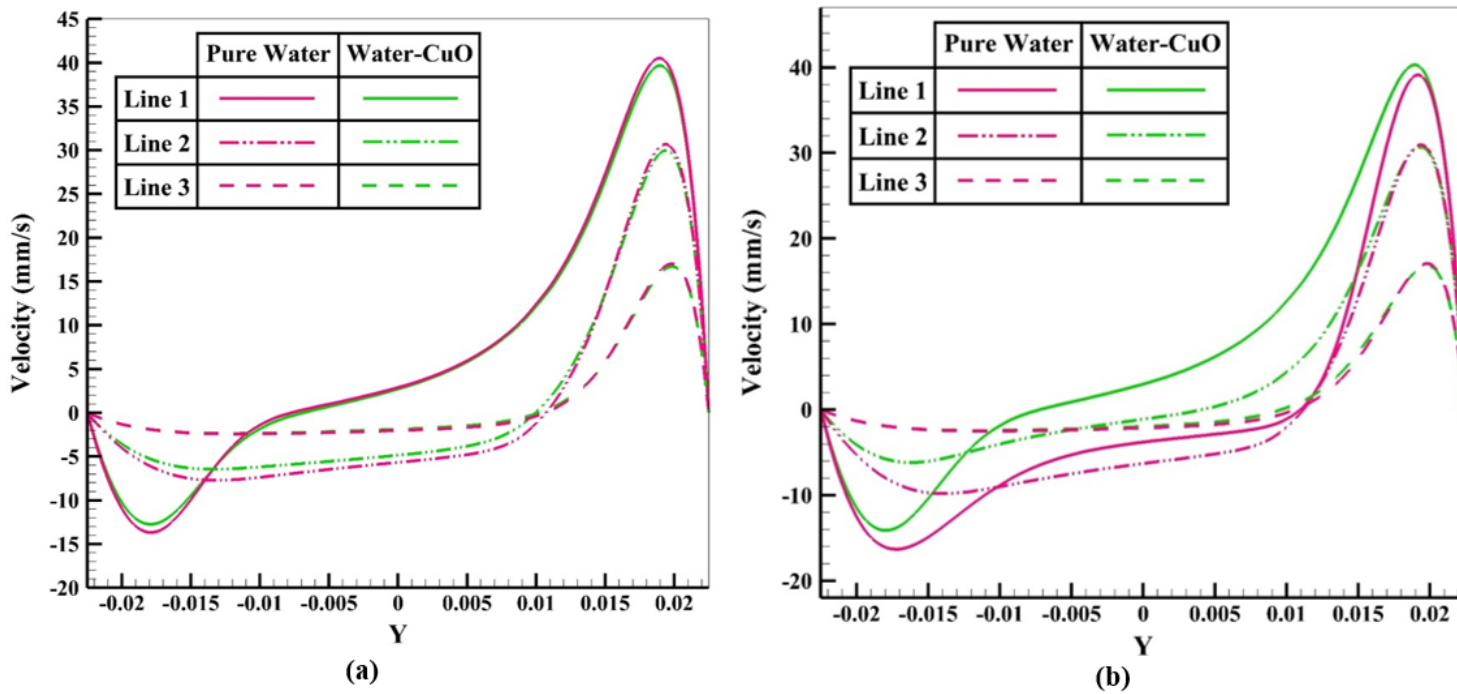
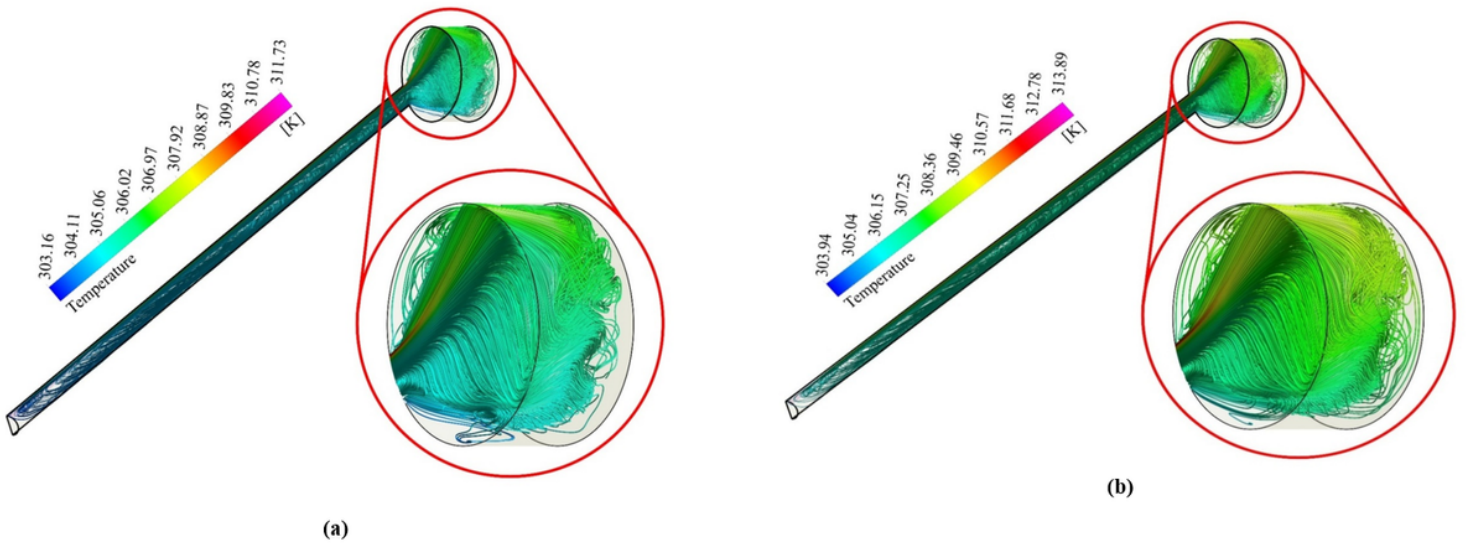


Figure 6

Distribution of velocity at various sections at (a) t=30 and (b) t=60 minutes



**Figure 7**

Distribution of temperature for pure water at (a)  $t=30$  and (b)  $t=60$  minutes

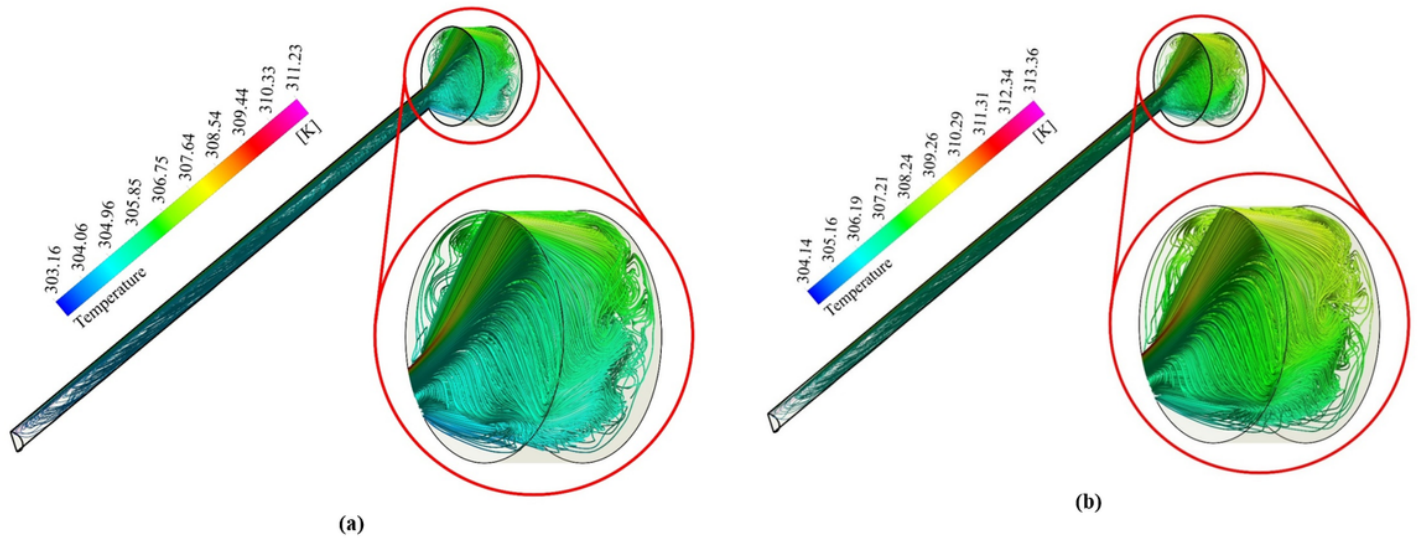


**Figure 8**

Distribution of temperature for nanofluid at (a)  $t=30$  and (b)  $t=60$  minutes

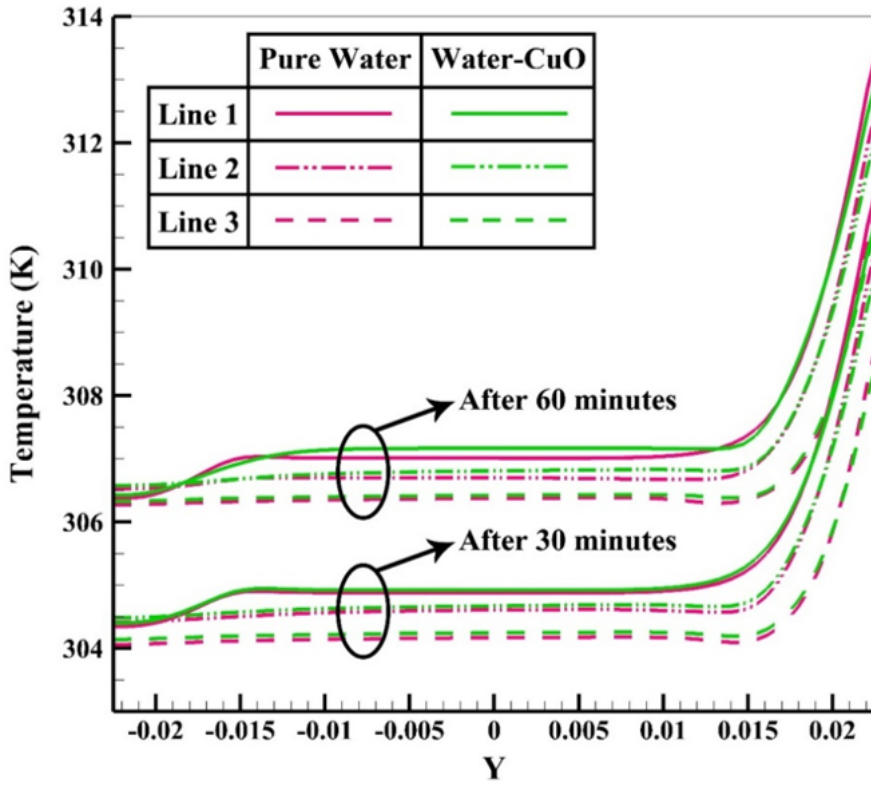


Figure 9

Distribution of temperature at various sections

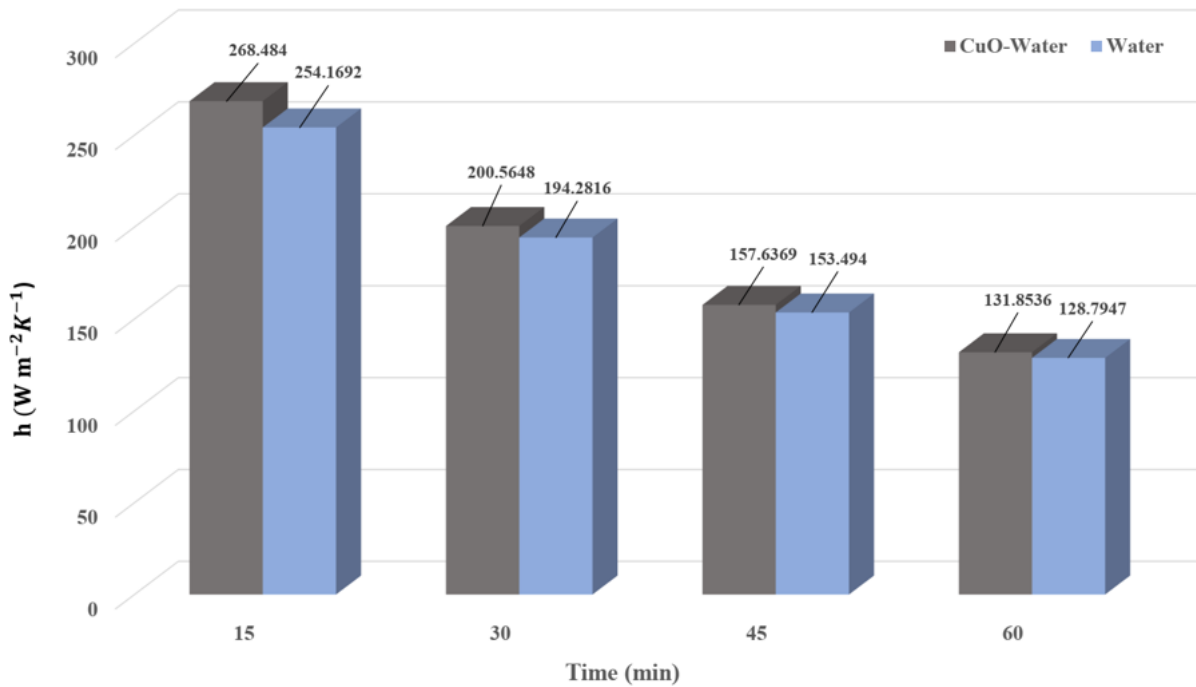
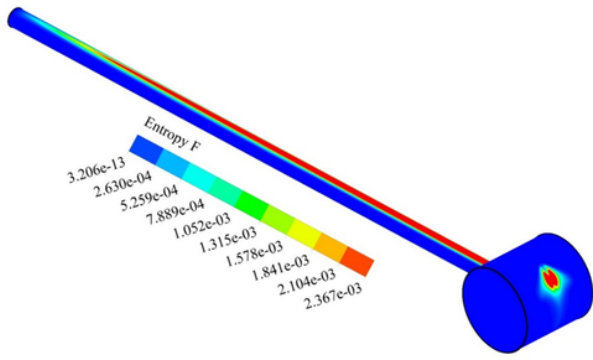
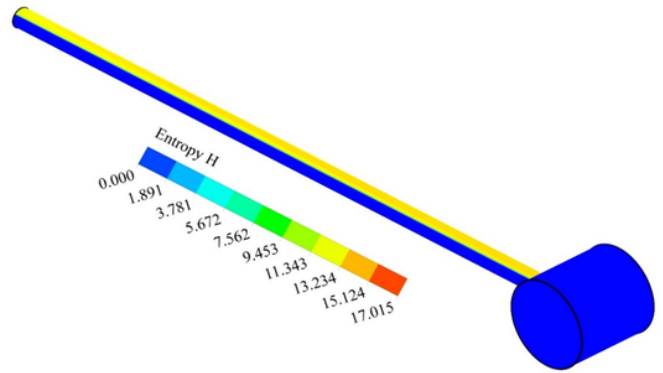


Figure 10

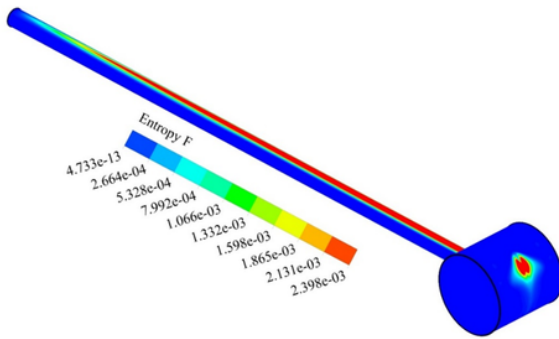
Comparison of heat transfer performance of the collector for water and nanofluid over the flow time



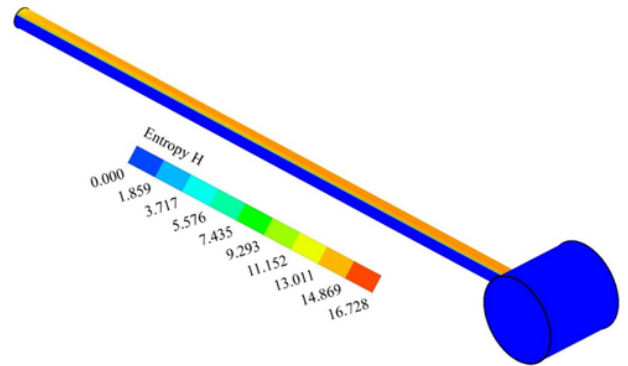
(a)



(b)



(c)



(d)

Figure 11

Distribution of  $S_{gen,f}$  (a)  $t=30$  and (c)  $t=60$  minutes,  $S_{gen,h}$  (b)  $t=30$  and (d)  $t=60$  minutes for pure water

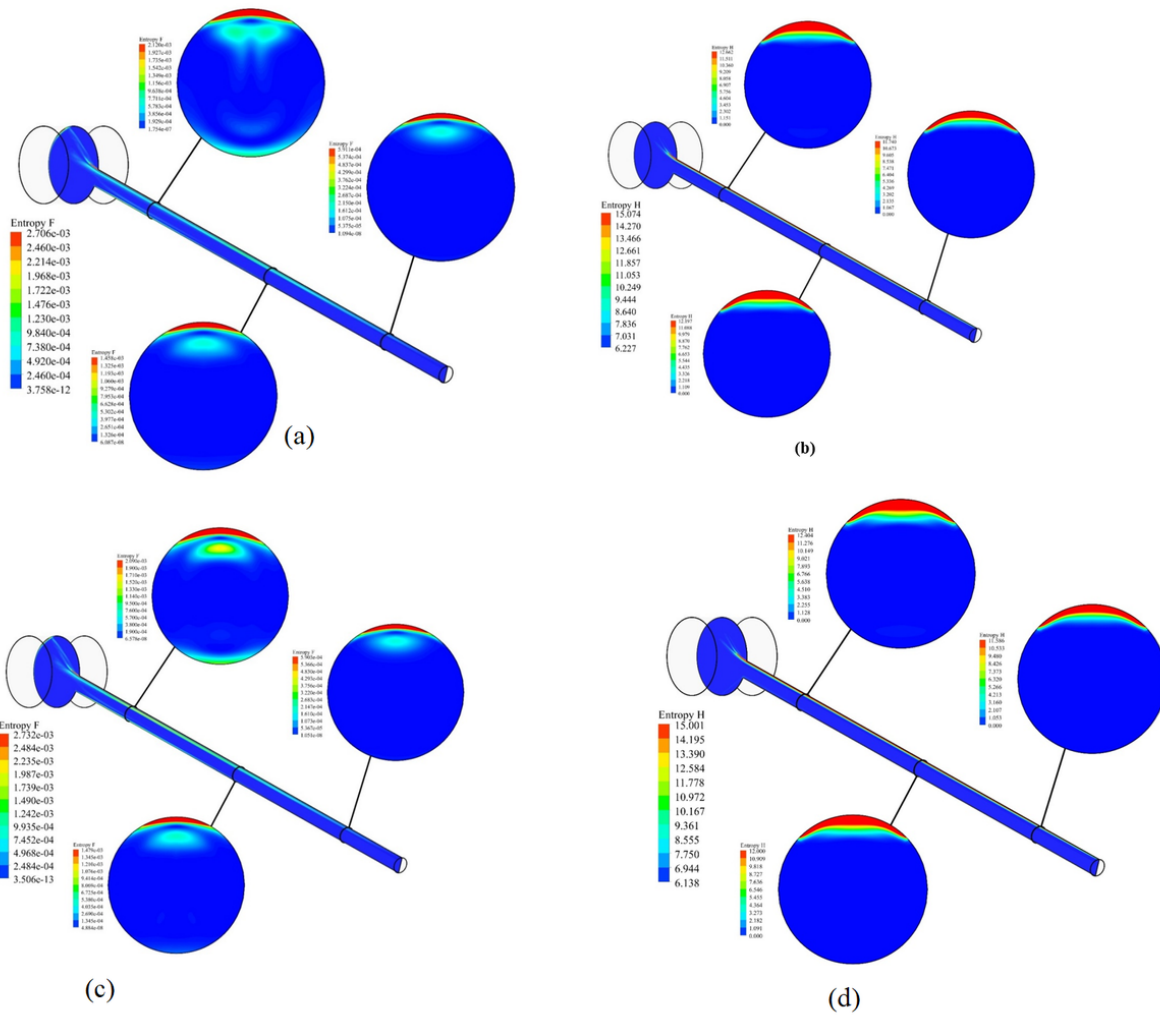
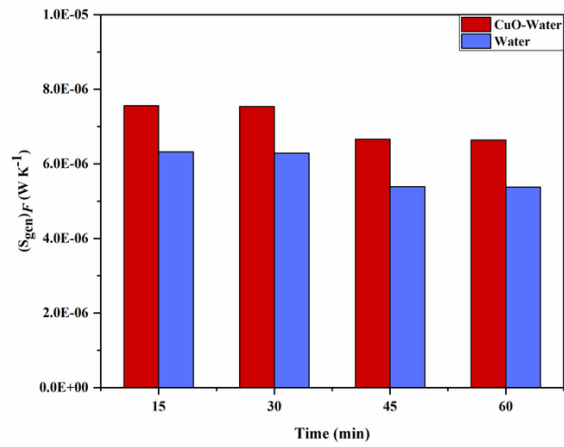
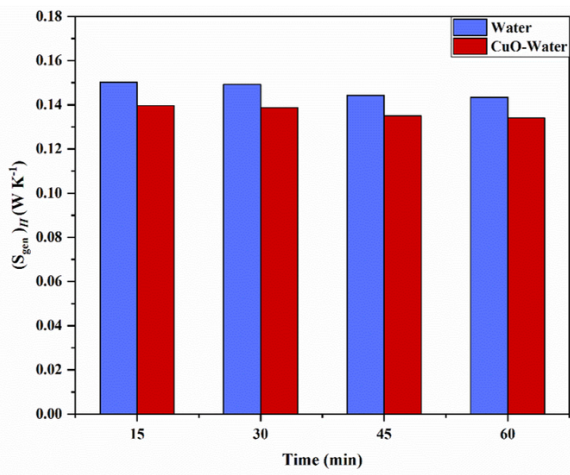


Figure 12

Distribution of  $S_{gen,f}$  (a)  $t=30$  and (c)  $t=60$  minutes,  $S_{gen,th}$  (b)  $t=30$  and (d)  $t=60$  minutes for nanofluid



(a)



(b)

Figure 13

Comparison of (a) fluid friction irreversibility and (b) heat transfer irreversibility for water and nanofluid